Park et al. *NPG Asia Materials* (2019) 11:32
https://doi.org/10.1038/s41427-019-0132-z

NPG Asia Materials

ARTICLE Open Access

Self-assembly of correlated (Ti, V)O_2 superlattices with tunable lamella periods by kinetically enhanced spinodal decomposition

Jaeseoung Park[1], Gi-Yeop Kim[1], Kyung Song[2], Si-Young Choi[1] and Junwoo Son[1]

Abstract

Spinodal decomposition, the spontaneous phase separation process of periodic lamellae at the nanometer scale, of correlated oxide ((Ti, V)O_2) systems offers a sophisticated route to achieve a new class of mesoscale structures in the form of self-assembled superlattices for possible applications using steep metal–insulator transitions. Here, we achieve the tunable self-assembly of (Ti, V)O_2 superlattices with steep transitions ($\Delta T_{MI} < 5$ K) by spinodal decomposition with accurate control of the growth parameters without conventional layer-by-layer growth. Abrupt compositional modulation with alternating Ti-rich and V-rich layers spontaneously occurs along the growth direction because in-plane lattice mismatch is smaller in this direction than in other directions. An increase in the film growth rate thickens periodic alternating lamellae; the phase separation can be kinetically enhanced by adatom impingement during two-dimensional growth, demonstrating that the interplay between mass transport and uphill diffusion yields highly periodic (Ti, V)O_2 superlattices with tunable lamellar periods. Our results for creating correlated (Ti, V)O_2 oxide superlattices provide a new bottom-up strategy to design rutile oxide tunable nanostructures and present opportunities to design new material platforms for electronic and photonic applications with correlated oxide systems.

Introduction

Superlattices, structures with periodic blocks on the nanometer scale, have realized unique properties unachievable with the use of a single layer via structural and electronic confinement effects[1–4]. While superlattices can be artificially fabricated using film growth with layer-by-layer control, self-assembly by thermodynamically driven phase separation provides a straightforward and simple route to naturally form superlattices[5,6], which leads to distinct physical properties (e.g., superconductivity[7], multiferroicity[8,9], and high ionic conductivity[10,11]) unobtainable in single-phase materials. When the materials are largely immiscible, the reaction-controlled phenomena involving nucleation and growth give rise to the phase separation process, and therefore, a large number of randomly distributed nuclei grow into a type of irregular nanodot-embedded nanocomposite (0D)[7] or nanopillar-embedded nanocomposite (1D)[8–11]. Unlike nucleation and growth, spinodal decomposition is a unique thermodynamic, diffusion-controlled phenomenon that leads to spontaneous formation of multiple phases from a uniform mixture, and the process occurs due to long-range spatial and periodic compositional modulations on the nanometer scale. This unique feature of spinodal decomposition has been exploited to obtain highly periodic nanostructures, e.g., self-assembled two-dimensional superlattices in III–V semiconductors[12–14], metal alloys[15,16], and transition metal oxides[17–19] systems.

Correspondence: Si-Young Choi (youngchoi@postech.ac.kr) or Junwoo Son (jwson@postech.ac.kr)
[1]Department of Materials Science and Engineering (MSE), Pohang University of Science and Technology (POSTECH), Pohang 37673, South Korea
[2]Materials Testing and Reliability Division, Korea Institute of Materials Science (KIMS), Changwon, South Korea

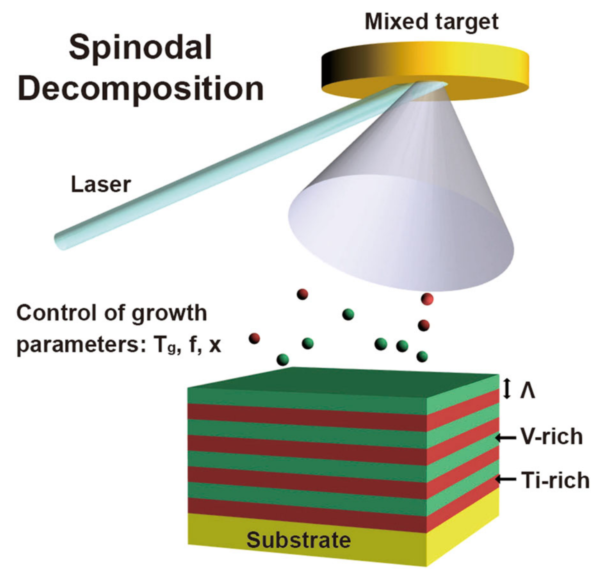

Fig. 1 Schematic of self-assembled (Ti, V)O_2 superlattice formation by spontaneous spinodal decomposition during PLD growth. The periods (Λ) and thicknesses of each layer could be accurately controlled by adjusting the growth parameters (growth temperature T_g, laser pulse frequency f, and target composition x)

Since TiO_2/VO_2 superlattices are uniquely composed of $3d^1$-correlated functional materials coupled with isostructural $3d^0$ insulators, they are predicted to have electrical and optical properties that can be tuned by external stimuli to provide a new platform for thin-film devices (i.e., half-metallic VO_2 slabs[20] and tunable metamaterials[19,21]). Layer-by-layer growth of TiO_2/VO_2 superlattices has been previously attempted, but the methods allowed excessive Ti diffusion into VO_2 layers and the formation of TiO_2 anatase polymorphs; therefore, these methods did not guarantee tunable and steep metal–insulator (MI) transition behavior in the superlattice[21].

The TiO_2/VO_2 system has been recently demonstrated in the bulk as an example of spinodal decomposition in the rutile oxide family. Spinodal decomposition occurs below 830 K if atomic diffusion is thermally activated[22]. This spinodal decomposition strongly depends on the crystallographic anisotropy that emerges from the anisotropic lattice parameters of a rutile oxide with tetragonal symmetry; compositional modulation of the lamellar structure preferentially appears normal to the c-axis rather than the a-axis because the lattice mismatch between TiO_2 and VO_2 is smaller along the a-axis (~1.5 %) than the c-axis (~3.7 %). In short, the formation of periodic Ti-rich and V-rich lamellae normal to the a-axis is the only option to minimize the elastic strain energy at the interfaces between two rutile phases, resulting in the generation of well-ordered superlattices [22,23].

Recently, for the application of tunable metamaterials, spinodal-decomposed (Ti, V)O_2 nanocomposite layers have been achieved by post-annealing[19], but these layers have an inferior structural order that was damaged by significant numbers of stacking faults and dislocations and by large variation among the lamellar periods; all of these traits can degrade the desirable properties of these nanocomposites. Furthermore, despite the potential importance of the accurate control of mesoscale dimensions in the (Ti, V)O_2 superlattices, there has been no promising method to tune the periodicity of a naturally assembled high-quality superlattice film by spinodal decomposition.

Here, we provide the first demonstration of self-assembled high-quality superlattices in (Ti, V)O_2 thin films from homogeneously mixed targets (Ti:V = x:1−x, x = 0.4, 0.5, and 0.55) and the precise control of lamellar periods (Λ) by adjusting the growth parameters of pulsed laser deposition (PLD) (Fig. 1). Unlike artificial superlattices that are assembled using layer-by-layer growth[21,24], alternating Ti-rich and V-rich layers with accurate thicknesses and atomically abrupt interfaces spontaneously formed by kinetically enhanced spinodal decomposition even without a post-annealing step. These traits yield abrupt MI transition characteristics ($\Delta T_{MI} <$ 5 K) with narrow hysteresis in superlattices ~50-nm thick. Lamellar periods induced by spinodal decomposition are highly tunable from 5.47 to 16.53 nm by adjusting the laser pulse frequency f to control the growth rate. This accurate control of spontaneous phase separation without post-annealing is attributed to the mass transport promoted by ion impingement during PLD growth and the consequent significant acceleration of uphill diffusion for spinodal decomposition. Therefore, our demonstration of producing self-assembled superlattices paves the way to design new superlattices with functionalities in nanoarchitectured materials that have strong correlations.

Results and discussion

The growth of self-assembled high-quality (Ti, V)O_2 superlattices

Epitaxial Ti-rich/V-rich (Ti, V)O_2 superlattices were grown on (001) TiO_2 substrates using a KrF pulsed laser to ablate a homogeneously mixed target (Fig. 1). Depending on the growth temperature T_g, the degree of the phase separation was significantly modulated at a constant laser pulse frequency (f = 7 Hz), target composition (Ti:V = 0.5:0.5), and oxygen partial pressure (10 mTorr). X-ray diffraction (XRD) results (Fig. 2a) indicate that films grown at low T_g (~200 °C) show a single (002) Bragg peak with thickness fringes around the (002) peak, which indicates a flat and homogeneous (Ti, V)O_2 solid solution. This result suggests that phase separation is kinetically suppressed at low T_g.

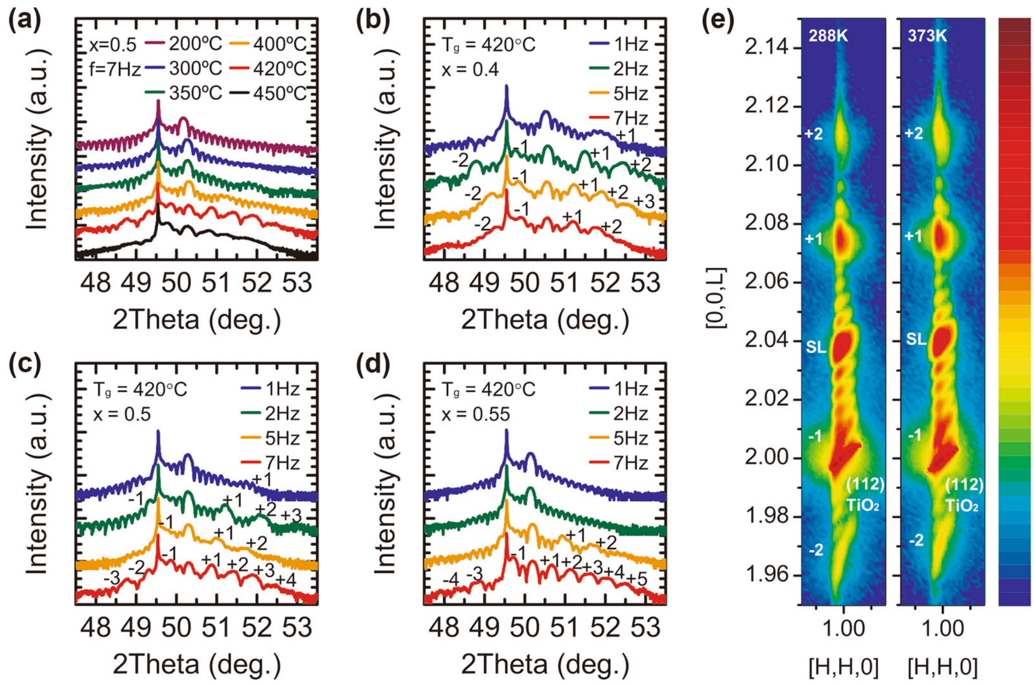

Fig. 2 Optimization of the self-assembled (Ti, V)O_2 superlattices. Symmetric θ–2θ scans of $Ti_xV_{1-x}O_2$ (x = 0.4, 0.5, and 0.55) epitaxial layers grown with different growth parameters. **a** (Ti, V)O_2 films with an average composition of $Ti_{0.5}V_{0.5}O_2$ grown at a laser pulse frequency f = 7 Hz at growth temperatures 200 ≤ T_g ≤ 450 °C. As T_g increased up to 420 °C, distinct satellite peaks up to fourth order, as well as thickness fringes, were observed. (Ti, V)O_2 films with average compositions of **b** $Ti_{0.4}V_{0.6}O_2$, **c** $Ti_{0.5}V_{0.5}O_2$, and **d** $Ti_{0.55}V_{0.45}O_2$ superlattices grown at 420 °C under 1 ≤ f ≤ 7 Hz. As f increased, the distance between adjacent satellite peaks was tuned. **e** Reciprocal space mapping (RSM) around the (112) reflection of the $Ti_{0.4}V_{0.6}O_2$ superlattice with nominal composition grown on (001) TiO_2 substrate f = 2 Hz at 420 °C

Figure 2a, interestingly, shows that the T_g of 420 °C results in distinct satellite peaks developing up to the fourth order, indicating that spontaneous phase separation occurs because atomic diffusion is thermally activated[19,22]. These higher-order satellite peaks never appear when the composition gradually changes along the interfaces of the superlattices, as reported in recent studies on (Ti, V)O_2 superlattices[19,21,24]. Therefore, the appearance of these high-order peaks at 420 °C suggests that the interfaces are sharp and that the superlattices are of high quality with composition modulations similar to a square wave along the c-axis. As T_g is further increased up to 450 °C, the satellite peaks and thickness fringes broaden and become unclear due to excess atomic diffusion from thermal energy. These characteristics are similar to those of randomly separated (Ti, V)O_2 thin films with inferior structural quality[19]. Based on our structural analysis, we infer that to obtain high-quality superlattices with abrupt interfaces and regular periodicity by spinodal decomposition, T_g must be precisely controlled between 400 and 450 °C.

From the position of the Bragg peaks, the estimated average out-of-plane lattice parameters were 2.924 Å in solid-solution films and 2.917 Å in superlattice films grown at the optimized T_g ~ 420 °C. This result suggests that the out-of-plane lattice parameter of the V-rich layer shrinks by coherently adhering to the Ti-rich layer that has a larger in-plane lattice parameter[22,24]. In addition, ω scans of the superlattices and solid solutions show similar full-width at half-maximum values; this similarity means that the two phases have a similar crystal quality (Fig. S1). Compositional modulation occurs selectively along the c-axis because the in-plane lattice mismatch between the V-rich and Ti-rich layers is smaller than the out-of-plane lattice mismatch. Thus, the preferred modulation direction is determined to minimize the strain energy at the interface between the two phases and yield a well-ordered superlattice[22]. Unlike spinodal decomposition of bulk (Ti, V)O_2 with a random distribution of periodicity (10–50 nm) and structural imperfections (e.g., incomplete stacking sequences or misfit dislocations)[22,23], the periodicity and thickness of each layer could be accurately controlled during PLD growth, resulting in better structural quality with coherent interfaces[19,22,23].

This method of assembling high-quality superlattices by spinodal decomposition during PLD growth is rapid; the process requires only a few minutes, unlike previous reports[19,22,23] on spinodal decomposition of (Ti, V)O_2 by post-annealing, which required at least several hours. We post-annealed our solid-solution $Ti_{0.5}V_{0.5}O_2$ films at

420 °C for more than 7 h, which is much longer than the growth time (a few minutes), but no satellite peak was observed (Fig. S2). Therefore, the results indicate that the periodic lamellar growth by PLD is caused by adatom kinetics during the PLD process rather than the thermodynamic stability.

To further understand how growth parameters influence the formation of well-ordered superlattices during PLD growth, *f* and target compositions were varied at the optimized T_g (~420 °C) (Fig. 2b–d). Almost all of these samples showed superlattice satellite peaks regardless of *f*. The exceptions were the samples grown from Ti:V = 0.55:0.45 target at $f = 1$ or 2 Hz (Fig. S3). However, as *f* was increased, the distance between adjacent satellite peaks was tuned. From the distance between adjacent satellite peaks, the thickness Λ [nm] of one period in the superlattices could be calculated as

$$\Lambda = \frac{m\lambda}{2(sin\theta_m + sin\theta_B)}$$

where m is the order of the satellite peak, λ is the X-ray wavelength, θ_m is the angle of the m^{th} order satellite peak, and θ_B is the average Bragg angle for the superlattice. Based on this relationship, Λ increased as *f* increased (5.69 nm at $f = 1$ Hz to 12.20 nm at $f = 7$ Hz in $Ti_{0.4}V_{0.6}O_2$; 5.47 nm at $f = 1$ Hz to 13.78 nm at $f = 7$ Hz in $Ti_{0.5}V_{0.5}O_2$; 10.41 at $f = 1$ Hz to 16.53 nm at $f = 7$ Hz in $Ti_{0.55}V_{0.45}O_2$) (Table S1). It should be noted that the samples grown from the Ti:V = 0.4:0.6 and Ti:V = 0.5:0.5 targets exhibit more of a tendency to undergo phase separation than those grown from Ti:V = 0.55:0.45, probably because both target compositions are in the range of the spinodal regions based on the TiO_2–VO_2 phase diagram[22].

To verify the epitaxial relationship in the self-assembled superlattices, XRD reciprocal space mapping (RSM) around the (112) TiO_2 Bragg peak of the self-assembled $Ti_{0.4}V_{0.6}O_2$ superlattice grown at 420 °C was performed below (~288 K) and above (~373 K) the MI transition temperature T_{MI} of VO_2 (Fig. 2e). The average *c*-axis lattice parameter of the superlattice decreased slightly from 2.903 to 2.900 Å as T_g increased; this reduction in the lattice parameter is evidence of a structural phase transition (monoclinic to rutile) of the phase-separated V-rich $Ti_xV_{1-x}O_2$ ($x \leq 0.2$) layers[22,24]. The second-order satellite peaks were clearly observed with the main Bragg peak of the superlattices along the q_z (out-of-plane) directions, which agrees with the results of the XRD θ-2θ scan. The substrate and superlattice peaks (i.e., Bragg peak and satellite peaks) had identical q_x values, which means that entire layers in the ~50-nm-thick superlattices are coherently strained by the rigid TiO_2 substrates despite the large lattice mismatch between the V-rich phase and the Ti-rich phase (or TiO_2 substrate).

Atomically ordered superlattices were confirmed by an atom-scale STEM analysis. As shown in Fig. 3a, V-rich layers with bright contrast alternate with Ti-rich layers, with abrupt interfaces on the (001) TiO_2 substrate. Although Ti and V have similar atomic numbers, the contrast between the alternating layers was significant in the high angle annular dark field (HAADF) images, probably as a result of strain effects[25,26], which causes more electron scattering in the less symmetric monoclinic V-rich layer than in the rutile Ti-rich layer. Along with the contrast in the HAADF images, a difference in the crystal symmetry was also observed between the lamellar structures. The Ti-rich layer is a high-symmetry rutile structure, but the FFT image of the V-rich layer shows diffraction spots of superstructures (right side of Fig. 3a, yellow circles); these spots indicate monoclinic structures due to the formation of the V^{4+} ion dimer[19,22,23]. Moreover, our self-assembled superlattices showed no defects at the interface, meaning that the alternating layers were fully strained with perfectly coherent interfaces, as predicted by the RSM analysis. The variation in the *c*-lattice and *a*-axis lattice parameters in each layer, $\Delta c/c$ *and* $\Delta a/a$, was extracted using GPA (geometric phase analysis, HREM Research Inc.), as shown in Fig. S4. The $\Delta c/c$ in the V-rich layer is approximately −0.03, which concurs with previous reports that the parameter is 3.0% larger in the Ti-rich layer than in the V-rich layer in phase-separated (Ti, V)O_2 created using spinodal decomposition[22,23]. On the other hand, the $\Delta a/a$ values of the in-plane lattice parameter of both Ti-rich and V-rich layers were coherently constrained by interactions with the rigid TiO_2 substrates in our superlattices (Fig. S4); as a result, tension could be significant only in the V-rich layers with negligible strain in the Ti-rich layers along the in-plane direction. With an assumption of Vegard's law[27], the $\Delta c/c$ in the V-rich layer, $V_{0.9}Ti_{0.1}O_2$, is expected to be approximately −0.027, and therefore, the actual strain in the V-rich layer is approximately −0.3% (compressive) along the out-of-plane direction. For better accuracy of the strain analysis, we measured the $\Delta c/c$ by using off-axis in-line holography TEM (Fig. S5)[28,29], wherein a much wider field of view can be used compared to the GPA method and the rigid TiO_2 can be used as a reference guaranteeing better accuracy. The $\Delta c/c$ values in the V-rich layers are approximately −0.023 except for the first V-rich layer having a $\Delta c/c$ value of approximately −0.019. Therefore, the strain in the V-rich layers is approximately +0.4% (tensile) along the out-of-plane direction, and the first V-rich layer exhibits a stronger tensile strain of ~0.8%. This structural modulation in our superlattices is inconsistent with previous reports on phase-separated bulk (Ti, V)O_2 with alternately stacked compressive Ti-rich and tensile V-rich layers[22,23].

Compositional modulations with sharp interfaces between alternating lamellae can be visualized directly by

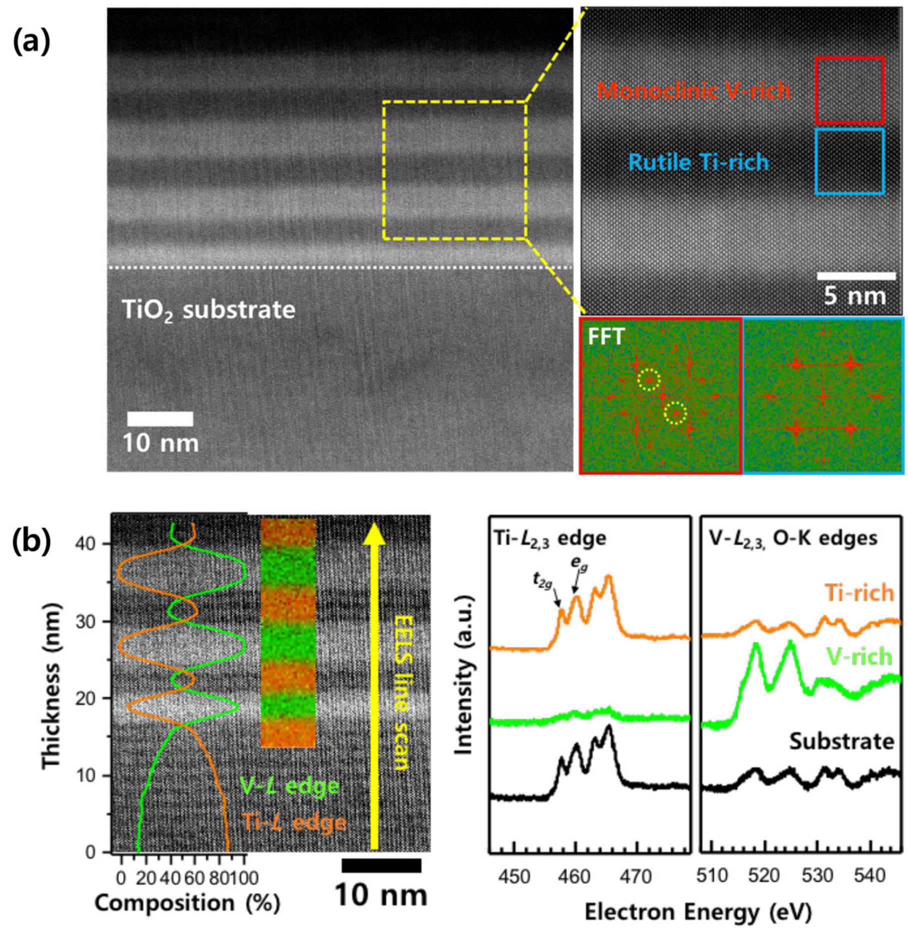

Fig. 3 Local structure of atomically ordered (Ti, V)O_2 superlattices. a Left: STEM-HAADF images of self-assembled (Ti, V)O_2 superlattices with $Ti_{0.4}V_{0.6}O_2$ average composition. Layers of V-rich (bright contrast) and Ti-rich (dark contrast) alternate with abrupt interfaces on the (001) TiO_2 substrate. Upper right: Magnified high-resolution STEM-HAADF image in the yellow square with dotted line. Lower right: Fast Fourier transformation (FFT) images of the monoclinic V-rich layer (red square) and the rutile Ti-rich layer (blue square). The FFT of the Ti-rich layers shows high-symmetry rutile structures, whereas the V-rich layers show diffraction spots of superstructures, which indicate the formation of monoclinic structures due to the formation of V^{4+} ion dimers. **b** EELS spectra mapping along the growth direction (yellow arrow) and the corresponding EELS spectra of the Ti-rich layer (orange), the V-rich layer (green), and TiO_2 substrate (black). Ti/V ratio of compositional modulation as a function of thickness estimated from the EELS spectra

detecting V L-edges (513−528 eV) and Ti L-edges (455−468 eV) using electron energy loss spectroscopy (EELS) and a corrected electron probe of 0.8 Å on a selected area (Fig. 3b). In the EELS spectra of the Ti-rich layer, the dominant peaks occur at 457.7 eV (L_3-edge) and 463.2 eV (L_2-edge); in the EELS spectra of the V-rich layer, the dominant peaks occur at 518.4 eV (L_3-edge) and 524.9 eV (L_2-edge). The 5.5 eV $L_{2,3}$-edge splitting in the Ti-rich layer and 6.5 eV $L_{2,3}$-edge in the V-rich layer are similar to those in previous XAS or EELS studies on rutile TiO_2 and monoclinic VO_2 systems[30–33]. As shown on the right side of Fig. 3b, the energy difference between t_{2g} and e_g in the Ti L_3-edge in the Ti-rich lamella is found to be ~2.1 eV[34], and the L_3/L_2 ratio in the V L-edges is comparable to 1[35]. Both of these results imply that the valence states of Ti and V are likely to be +4. Therefore, Ti and V maintain their original valence states, and thus, there should be almost no atomic scale defects (i.e., oxygen vacancies) decreasing the valence states of Ti and V. The weak signals of the Ti $L_{2,3}$-edges in the V-rich layers and the weak signals of the V $L_{2,3}$-edges in the Ti-rich layers indicate that the phases are only slightly soluble in each other, so the local composition profile can be estimated from the relative intensity of the dominant and minor EELS signals of each layer. The EELS spectra suggest that the V-rich layers are likely to be $Ti_{0.1}V_{0.9}O_2$ and that the Ti-rich layers are likely to be $Ti_{0.6}V_{0.4}O_2$. These compositions match well with those of the separated phases in bulk polycrystalline or single-crystal $Ti_{0.4}V_{0.6}O_2$ at T_g ~ 420 °C by spinodal decomposition[22,23]. Λ, i.e., the sum of the

V-rich layer and Ti-rich layer thickness, observed in the STEM image was estimated to be ~8.9 nm, which is comparable to the value of ~8.6 nm estimated using the satellite peak of the XRD pattern.

Abrupt MI transition in self-assembled (Ti, V)O_2 superlattices

The degree of phase separation in our periodic (Ti, V) O_2 superlattices obtained by spinodal decomposition was further explored using temperature-dependent sheet resistance R_S measurements (Fig. 4). Indeed, electrical transport in (Ti, V)O_2 superlattices was highly correlated with the self-assembly of (Ti, V)O_2 by spinodal decomposition. In the solid solution of $Ti_{0.5}V_{0.5}O_2$ grown at 200 °C, which is kinetically suppressed due to insufficient atomic diffusion, the insulating state was maintained without an MI transition. However, as T_g increased, sufficient thermal energy was supplied to drive the thermodynamically stable phase separation of Ti-rich and V-rich phases; thus, an abrupt MI transition induced by the V-rich phase appeared at T_{MI} with an orders of magnitude change in the R_S of the superlattices grown at the optimized $T_g \sim 420$ °C for phase separation (Fig. 4a). Thus, phase separation in the superlattices is required for the MI transition in electrical transport.

Furthermore, since the XRD results suggest that the growth rate affected the degree of phase separation of the superlattice, the change in the MI transition was investigated in the self-assembled superlattices grown under different laser frequencies ($1 \leq f \leq 7$ Hz) with different Ti mole fractions ($x = 0.4$, 0.5, and 0.55) of targets at $T_g \sim 420$ °C (Fig. 4b–d). The insulating phase without an MI transition appeared only in the $Ti_{0.55}V_{0.45}O_2$ samples grown at $f = 1$ or 2 Hz; this result is consistent with the absence of satellite peaks in the XRD patterns. In all other samples, the MI transition occurred, but the abrupt MI transition tended to be suppressed as f decreased, which indicated that the growth rates substantially affect the steepness of the MI transition in the self-assembled (Ti, V)O_2 superlattices.

The increase in the thickness of the V-rich lamellae with an increase in f suggests that increasing the thickness of the V-rich layers induced by spinodal decomposition favors an increase in the steepness of the MI transition. To quantify how the thickness of the V-rich phase affected electrical transport, the nominal thickness of the V-rich layer was quantitatively calculated based on the superlattice periods and the lever rule (Table S2). Universally, the abrupt transition was suppressed when the calculated thickness of the phase-separated V-rich layer was less than a critical thickness of ~3 nm due to the slight interdiffusion between Ti and V atoms along both layers, which was also previously observed in

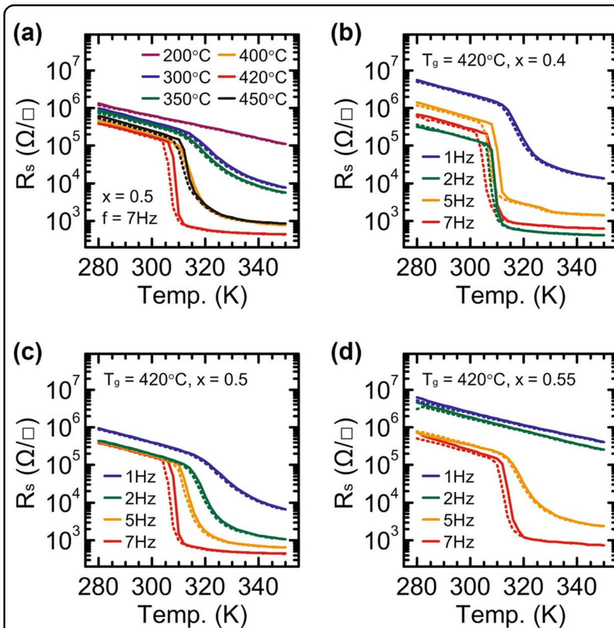

Fig. 4 Metal–insulator transition characteristics in self-assembled (Ti, V)O_2 superlattices. Temperature-dependent sheet resistance R_S in the $Ti_xV_{1-x}O_2$ ($x = 0.4$, 0.5, and 0.55) superlattice with nominal composition grown with different growth parameters. **a** (Ti, V)O_2 films with an average composition of $Ti_{0.5}V_{0.5}O_2$ grown at laser pulse frequency $f = 7$ Hz over a range of growth temperatures of $200 \leq T_g \leq 450$ °C. (Ti, V)O_2 films with an average composition of **b** $Ti_{0.4}V_{0.6}O_2$, **c** $Ti_{0.5}V_{0.5}O_2$, and **d** $Ti_{0.55}V_{0.45}O_2$ grown at 420 °C and $1 \leq f \leq 7$ Hz

$((TiO_2)_m/(VO_2)_n)_r$ superlattices[24] and ultrathin epitaxial VO_2 thin films[25,36] on a (001) TiO_2 substrate.

Interestingly, the MI transition of self-assembled superlattices is steeper ($\Delta T_{MI} < 5$ K) than that of the $((TiO_2)_m/(VO_2)_n)_r$ superlattices[24] or Ti-doped VO_2 epitaxial thin films[37], and this difference is ascribed to the chemically abrupt interface between the V-rich and Ti-rich phases in our superlattices. Along with the steep MI transition in our self-assembled superlattices, the T_{MI} of the superlattices (313–307 K) was consistently ~30 K less than that in bulk VO_2 regardless of the average compositions of the superlattices. Because Ti doping in VO_2 is known to increase T_{MI}[22], Ti doping is unlikely to be the origin of the reduced T_{MI} in our case. Rather than doping issues, the homogeneously accumulated tensile strain in the superlattice film mainly contributes to the reduction in T_{MI} because both V-rich and Ti-rich lamellae formed on the rigid TiO_2 substrate, as demonstrated in RSM (Fig. 2e)[38].

We found another interesting issue in our superlattice VO_2 film. Single VO_2 (or V-rich) epitaxial films are usually relaxed on a TiO_2 substrate due to the high tensile strain when the films are thicker than 15 nm (i.e., the critical thickness for a strained VO_2 single layer), which is accompanied by the line cracks[25,38–41] that substantially disturb the abrupt MI transition of this correlated oxide. Although thick VO_2 films that retain the abrupt MI transition can be achieved on a (001) TiO_2 substrate by inserting a buffer layer (SnO_2), the films are relaxed in a different way by texturing columnar VO_2 structures without any line cracks[42]. Therefore, obtaining crack-free and strained films thicker than 15 nm with abrupt MI transitions has been a difficult challenge. Surprisingly, our ~50-nm-thick self-assembled superlattices are fully strained and exhibit no cracks (Fig. S1), which are attributed to the fully strained ultrathin V-rich layers sandwiched by Ti-rich bottom and top layers; this crack-free structure leads to single-step steep temperature-dependent MIT with a decreased MI transition temperature (T_{MI}) (Fig. 4) for electrical transport, which cannot be achieved in single V-rich epitaxial films[39] and even in $(TiO_2)_m/(VO_2)_n$ superlattices obtained by layer-by-layer growth[43].

Mechanism of the formation of self-assembled (Ti, V)O_2 superlattices during growth

To elucidate the formation mechanisms of the self-assembled superlattices during PLD growth in (Ti, V)O_2 systems, Λ was plotted as a function of the growth rate, which is controlled by f, for superlattices with different Ti/V ratios (Fig. 5a). In all cases, Λ increased linearly as the growth rate increased, regardless of the Ti/V ratio, indicating that sufficient energy for atomic diffusion is available with the increasing growth rate[9,44,45]. If spinodal decomposition is determined by the thermal uphill diffusion as a basic process leading to phase separation, Λ should decrease as the growth rate increases based on conventional spinodal decomposition[45]; this is contrary to the observations; thus, in our case, some factor other than thermal diffusion determines Λ[45].

During film growth, mass transport by ion impingement, as well as uphill thermal diffusion for spinodal decomposition, has a strong contribution to Λ. Ion impingement during PLD growth lowers the activation energy for mass transport of spinodal decomposition according to the following equation[15,17]:

$$D^* = D_0 \exp\left(-\frac{Q^*}{kT}\right)$$

where $Q^* = Q - \alpha I$, D^* represents the increased diffusion coefficient, D_0 is the initial diffusivity, Q is the activation energy without ion impingement, $0 < \alpha < 1$ is a constant and I is the energy flux from ion impingement. Therefore, the increased energy flux with increasing laser pulse frequency would reduce Q^* for uphill diffusion; the reduction in Q^* causes an increase in the diffusion coefficient and accordingly increases the period of the superlattices. The increased mass transport (i.e., diffusivity) by ion impingement from the PLD plume seems to reduce the activation energy for atomic diffusion and thus should be a more dominant mechanism than thermal diffusion in our case. Indeed, estimates of Q^* for spontaneous formation of our superlattices were in the range from 0.436 to 0.574 eV, which are much smaller than that reported for Ti diffusion in a rutile TiO_2 system ($1.0 \le Q^* \le 1.2$ eV)[46,47] (Fig. 5b). Furthermore, the estimated Q^* decreased as f (i.e., the growth rate) increased (e.g., 0.574 ± 0.011 eV at $f = 3$ Hz to 0.436 ± 0.078 eV at $f = 7$ Hz); this change may occur because the vanadium and

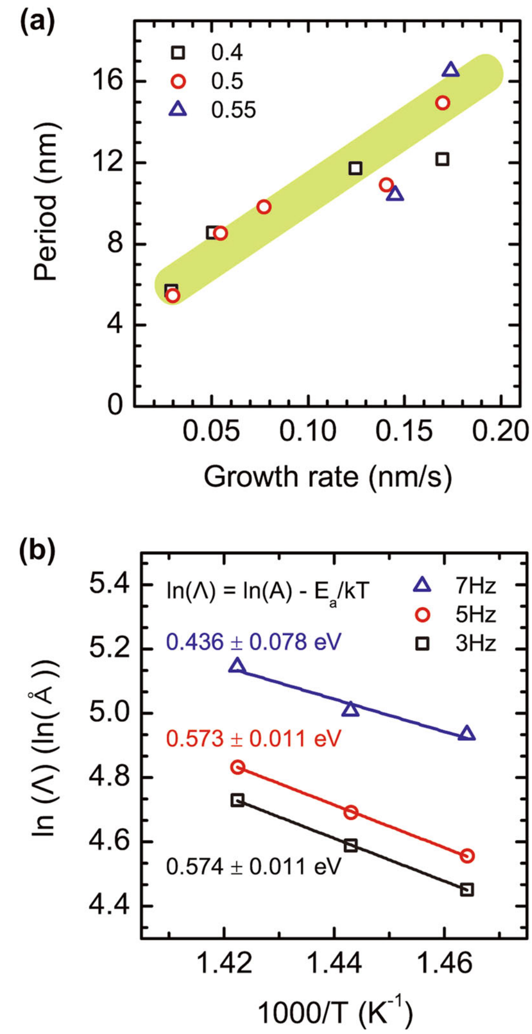

Fig. 5 Characterization of spontaneous superlattice formation. a Change in periods Λ with growth rate in self-assembled $Ti_xV_{1-x}O_2$ (x = 0.4, 0.5, and 0.55) superlattices. The growth rate was calculated by dividing the total thickness by the growth time. Λ increased as the growth rate increased. **b** Arrhenius plot of Λ in $Ti_{0.5}V_{0.5}O_2$ superlattices with different laser frequencies f. The activation energy decreased from 0.574 ± 0.011 eV at $f = 3$ Hz to 0.436 ± 0.078 eV at $f = 7$ Hz; the change is attributed to a considerable increase in mass transport during impingement by V and Ti ions generated by the excimer laser

titanium ions formed by the focused excimer laser considerably increased mass transport during ion impingement[48]. Because thin-film epitaxy is a nonequilibrium process governed by a competition between kinetics and thermodynamics, the acceleration of kinetics by ion impingement enables the formation of spontaneously ordered superlattices without long thermal annealing times; this process cannot be achieved by bulk synthesis under an equilibrium process[17,18].

Conclusions

In summary, we have successfully demonstrated the creation of high-quality self-assembled (001) $Ti_xV_{1-x}O_2$ ($x = 0.4$, 0.5, and 0.55) superlattices with tunable periods by kinetically enhanced spinodal decomposition driven by ion-impingement effects during PLD growth. The superlattice period Λ could be accurately and uniformly controlled from 5.47 to 16.53 nm by varying the laser pulse frequency ($1 \le f \le 7$ Hz) at the optimized growth temperature (420 °C) with three compositions of targets ($x =$ 0.4, 0.5, and 0.55). Λ increased as f (i.e., growth rate) increased; as a result, the MI transition in the superlattices became steeper. The increased mass transport due to ion-impingement effects reduces the activation energy and increases the diffusion coefficients for spinodal decomposition, so highly periodic (Ti, V)O_2 superlattices with tunable lamella periods can be produced in a relatively short time. These results provide a new strategy for bottom-up design of correlated (Ti, V)O_2 oxide superlattices as a new platform material for electronic and photonic applications.

Materials and methods

The growth of self-assembled heteroepitaxial $Ti_xV_{1-x}O_2$ ($x = 0.4$, 0.5, and 0.55) superlattices

Epitaxial Ti-rich/V-rich (Ti, V)O_2 superlattices with thicknesses of 44–55 nm were grown on (001) TiO_2 substrates using PLD (Coherent Compex Pro 102F) to ablate homogeneously mixed targets. The stoichiometric targets for PLD growth were prepared by sintering dry-milled stoichiometric powders of V_2O_5 (99.99%, Sigma-Aldrich) and TiO_2 (99.95%, Sigma-Aldrich) at 600 °C for 6 h. The compositions of these targets ($x = 0.4$, 0.5, and 0.55) were analyzed by energy-dispersive X-ray spectroscopy using high-resolution FE-SEM (JSM 7401F, JEOL). The (001) TiO_2 single crystal substrates (Shinkosha) were loaded onto the substrate holder in the PLD chamber, which was then evacuated to a base pressure of $\sim 5 \times 10^{-7}$ Torr. Then, the rotating targets were ablated by focusing a KrF excimer laser ($\lambda = 248$ nm) with a fluence of 1 J/cm^2 and various pulse repetition rates ($1 \le f \le 7$ Hz). The growth was performed at a fixed oxygen partial pressure of ~10 mTorr with various substrate temperatures of $200 \le T_g \le 450$ °C, which were accurately controlled by placing a thermocouple in the cavity of the substrate holder. After growth, the samples were cooled to room temperature at a rate of 20 °C/min.

Materials characterization

For structural characterization, high-resolution X-ray scattering measurements (symmetric 2θ-ω scan and asymmetric RSM) were conducted using synchrotron radiation ($\lambda = 0.15401$ nm, energy = 10 keV) at the 3D XRD beamline of the Pohang Light Source-II. Out-of-plane and in-plane lattice parameters were also measured using an HRXRD (Discover 8, Bruker).

The STEM sample was prepared by mechanically grinding samples to a thickness of ~70 μm, dimpling them to a thickness of ~10 μm, and then ion milling the samples using Ar^+. HAADF-STEM analysis was performed using a STEM (JEM-2100F, JEOL) at 120 kV equipped with an aberration corrector (CEOS GmbH). For chemical analysis, an EELS line scan was performed using an EEL spectrometer (GIF Quantum spectrometer, Gatan) with a dispersion range of 0.05 eV and dual EELS mode for the Ti L- and V L-edges. The collection semiangle from the HAADF detector under 120 kV ranged from 50 to 160 mrad, and the convergence semiangle for EELS acquisition was 15 mrad. All HAADF-STEM images were bandpass filtered to reduce background noise (HREM Research Inc.).

Electronic characterization for sheet resistance versus temperature was performed in the van der Pauw geometry during heating and cooling from 280 to 350 K with square samples (5 × 5 mm) and indium ohmic contacts (<1 × 1 mm) in the sample corners. The four-terminal resistances were measured with a 1 μA current.

Acknowledgements

J.S. and J.P. acknowledge support for this work from the Basic Science Research Program (2017R1A2B2007819 and 2017M2A2A6A01020116) and the Creative Materials Discovery Program (2018M3D1A1058997) through the National Research Foundation of Korea (NRF) funded by the Ministry of Science and ICT and by the Ministry of Trade, Industry and Energy (10076608). K.S. acknowledge support of the National Research Foundation of Korea (NRF, 2018R1A2B6008258). S.-Y.C. and G.-Y.K. acknowledge the support of the Global Frontier Hybrid Interface Materials of the National Research Foundation of Korea (NRF) funded by the Ministry of Science and ICT (2013M3A6B1078872). In addition, this study was partially supported by the Brain Korea 21 PLUS project (Center for Creative Industrial Materials).

Author contributions

J.S. and J.P. conceived the idea and designed the study. J.P. performed the film growth and processing, X-ray diffraction, transport measurements, AFM and analyzed the data under the supervision of J.S. G.-Y.K., K.S., and S.-Y.C. characterized the samples by scanning transmission electron microscopy. J.P., S.-Y.C., and J.S. wrote the manuscript, and all the authors commented on it.

Conflict of interest

The authors declare that they have no conflict of interest.

Publisher's note

Springer Nature remains neutral with regard to jurisdictional claims in published maps and institutional affiliations.

Supplementary information is available for this paper at https://doi.org/10.1038/s41427-019-0132-z.

Received: 12 August 2018 Accepted: 24 April 2019.
Published online: 28 June 2019

References

1. Nakamura, S., Senoh, M., Iwasa, N. & Nagahama, S. High-power ingan single-quantum-well-structure blue and violet light-emitting-diodes. *Appl. Phys. Lett.* **67**, 1868–1870 (1995).
2. Lee, H. N., Christen, H. M., Chisholm, M. F., Rouleau, C. M. & Lowndes, D. H. Strong polarization enhancement in asymmetric three-component ferroelectric superlattices. *Nature* **434**, 792–792 (2005).
3. Gibert, M., Zubko, P., Scherwitzl, R., Iniguez, J. & Triscone, J. M. Exchange bias in $LaNiO_3$-$LaMnO_3$ superlattices. *Nat. Mater.* **11**, 195–198 (2012).
4. Son, J., LeBeau, J. M., Allen, S. J. & Stemmer, S. Conductivity enhancement of ultrathin $LaNiO_3$ films in superlattices. *Appl. Phys. Lett.* **97**, 202109 (2010).
5. Nan, C. W. & Jia, Q. X. Obtaining ultimate functionalities in nanocomposites: design, control, and fabrication. *MRS Bull.* **40**, 719–723 (2015).
6. Zhang, W. R., Ramesh, R., MacManus-Driscoll, J. L. & Wang, H. Y. Multifunctional, self-assembled oxide nanocomposite thin films and devices. *MRS Bull.* **40**, 736–745 (2015).
7. Llordes, A. et al. Nanoscale strain-induced pair suppression as a vortex-pinning mechanism in high-temperature superconductors. *Nat. Mater.* **11**, 329 (2012).
8. Zheng, H. et al. Multiferroic $BaTiO_3$-$CoFe_2O_4$ nanostructures. *Science* **303**, 661–663 (2004).
9. Zheng, H. et al. Self-assembled growth of $BiFeO_3$–$CoFe_2O_4$ nanostructures. *Adv. Mater.* **18**, 2747–2752 (2006).
10. Yang, S. M. et al. Strongly enhanced oxygen ion transport through samarium-doped CeO_2 nanopillars in nanocomposite films. *Nat. Commun.* **6**, 8588 (2015).
11. Lee, S. et al. Strain tuning and strong enhancement of ionic conductivity in $SrZrO_3$–RE_2O_3 (RE = Sm, Eu, Gd, Dy, and Er) nanocomposite films. *Adv. Funct. Mater.* **25**, 4328–4333 (2015).
12. Eltoukhy, A. & Greene, J. Ion-bombardment-enhanced diffusion during the growth of sputtered superlattice thin films. *Appl. Phys. Lett.* **33**, 343–345 (1978).
13. Gallardo-Hernández, S. et al. Self-assembly of compositionally modulated $Ga_{1-x}Mn_xAs$ multilayers during molecular beam epitaxy. *Appl. Phys. Lett.* **103**, 192113 (2013).
14. Gao, M. et al. Spontaneous compositional superlattice and band-gap reduction in Si-doped $Al_xGa_{1-x}N$ epilayers. *Appl. Phys. Lett.* **87**, 191906 (2005).
15. Chen, C., Pei, Y., Shaha, K. & De Hosson, J. T. M. Tunable self-organization of nanocomposite multilayers. *Appl. Phys. Lett.* **96**, 073103 (2010).
16. He, J., Carosella, C., Hubler, G., Qadri, S. & Sprague, J. Bombardment-induced tunable superlattices in the growth of Au-Ni films. *Phys. Rev. Lett.* **96**, 056105 (2006).
17. Wakiya, N. et al. Magnetic-field-induced spontaneous superlattice formation via spinodal decomposition in epitaxial strontium titanate thin films. *NPG Asia Mater.* **8**, e279 (2016).
18. Takahashi, R. et al. Long-range spontaneous structural ordering in barium stannate thin films. *Appl. Phys. Lett.* **97**, 081906 (2010).
19. Chen, Z. et al. Self-assembled, nanostructured, tunable metamaterials via spinodal decomposition. *ACS Nano* **10**, 10237–10244 (2016).
20. Pardo, V. & Pickett, W. E. Half-metallic semi-Dirac-point generated by quantum confinement in TiO_2/VO_2 nanostructures. *Phys. Rev. Lett.* **102**, 166803 (2009).
21. Krishnamoorthy, H. N., Zhou, Y., Ramanathan, S., Narimanov, E. & Menon, V. M. Tunable hyperbolic metamaterials utilizing phase change heterostructures. *Appl. Phys. Lett.* **104**, 121101 (2014).
22. Hiroi, Z. et al. Spinodal decomposition in the TiO_2–VO_2 system. *Chem. Mater.* **25**, 2202–2210 (2013).
23. Hiroi, Z., Yoshida, T., Yamaura, J. & Okamoto, Y. Spinodally decomposed nanostructures in a TiO_2–VO_2 crystal. *APL Mater.* **3**, 062508 (2015).
24. Shibuya, K., Kawasaki, M. & Tokura, Y. Metal-insulator transitions in TiO_2/VO_2 superlattices. *Phys. Rev. B* **82**, 205118 (2010).
25. Paik, H. et al. Transport properties of ultra-thin VO_2 films on (001) TiO_2 grown by reactive molecular-beam epitaxy. *Appl. Phys. Lett.* **107**, 163101 (2015).
26. Tashman, J. et al. Epitaxial growth of VO_2 by periodic annealing. *Appl. Phys. Lett.* **104**, 063104 (2014).
27. Vegard, L. Die Konstitution der Mischkristalle und die Raumfüllung der Atome. *Z. Phys.* **5**, 17–26 (1921).
28. Koch, C. T. & Lubk, A. Off-axis and inline electron holography: a quantitative comparison. *Ultramicroscopy* **110**, 460–471 (2010).
29. Song, K. et al. Direct imaging of the electron liquid at oxide interfaces. *Nat. Nanotechnol.* **13**, 198-+ (2018).
30. Brydson, R. et al. Electron energy loss and X-ray absorption spectroscopy of rutile and anatase: a test of structural sensitivity. *J. Phys. Condens. Matter* **1**, 797 (1989).
31. Thomas, A. et al. Comparison of the electronic structure of anatase and rutile TiO_2 single-crystal surfaces using resonant photoemission and X-ray absorption spectroscopy. *Phys. Rev. B* **75**, 035105 (2007).
32. Abe, H., Terauchi, M., Tanaka, M., Shin, S. & Ueda, Y. Electron energy-loss spectroscopy study of the metal-insulator transition in VO_2. *Jpn. J. Appl. Phys.* **36**, 165 (1997).
33. Lin, X., Wang, Y., Dravid, V., Michalakos, P. & Kung, M. Valence states and hybridization in vanadium oxide systems investigated by transmission electron-energy-loss spectroscopy. *Phys. Rev. B* **47**, 3477 (1993).
34. Tominaka, S., Yoshikawa, H., Matsushita, Y. & Cheetham, A. K. Topotactic reduction of oxide nanomaterials: unique structure and electronic properties of reduced TiO_2 nanoparticles. *Mater. Horiz.* **1**, 106–110 (2014).
35. Zhou, H., Chisholm, M. F., Yang, T. H., Pennycook, S. J. & Narayan, J. Role of interfacial transition layers in VO_2/Al_2O_3 heterostructures. *J. Appl. Phys.* **110**, 073515 (2011).
36. Quackenbush, N. et al. Nature of the metal insulator transition in ultrathin epitaxial vanadium dioxide. *Nano Lett.* **13**, 4857–4861 (2013).
37. Muraoka, Y. *et al.* Spectroscopic evidence of the formation of $(V, Ti)O_2$ solid solution in VO_2 thinner films grown on TiO_2 (001) substrates. *J. Appl. Phys.* **109**, 043702 (2011).
38. Muraoka, Y. & Hiroi, Z. Metal-insulator transition of VO_2 thin films grown on TiO_2 (001) and (110) substrates. *Appl. Phys. Lett.* **80**, 583–585 (2002).
39. Nagashima, K., Yanagida, T., Tanaka, H. & Kawai, T. Stress relaxation effect on transport properties of strained vanadium dioxide epitaxial thin films. *Phys. Rev. B* **74**, 172106 (2006).
40. Fan, L. et al. Strain dynamics of ultrathin VO_2 film grown on TiO_2 (001) and the associated phase transition modulation. *Nano Lett.* **14**, 4036–4043 (2014).
41. Katase, T., Endo, K. & Ohta, H. Thermopower analysis of metal-insulator transition temperature modulations in vanadium dioxide thin films with lattice distortion. *Phys. Rev. B.* **92**, 035302 (2015).
42. Lee, D. et al. Sharpened VO_2 phase transition via controlled release of epitaxial strain. *Nano Lett.* **17**, 5614–5619 (2017).
43. Shibuya, K., Kawasaki, M. & Tokura, Y. Metal-insulator transitions in TiO_2/VO_2 superlattices. *Phys. Rev. B.* **82**, 205118 (2010).
44. Lu, Y. et al. Microstructure map for self-organized phase separation during film deposition. *Phys. Rev. Lett.* **109**, 086101 (2012).
45. Daruka, I. & Tersoff, J. Self-assembled superlattice by spinodal decomposition during growth. *Phys. Rev. Lett.* **95**, 076102 (2005).
46. Wendt, S. et al. The role of interstitial sites in the Ti3d defect state in the band gap of titania. *Science* **320**, 1755–1759 (2008).
47. Zhang, Z. et al. Unraveling the diffusion of bulk Ti interstitials in rutile TiO_2 (110) by monitoring their reaction with O adatoms. *J. Phys. Chem. C* **114**, 3059–3062 (2010).
48. De Giacomo, A., Shakhatov, V. & De Pascale, O. Optical emission spectroscopy and modeling of plasma produced by laser ablation of titanium oxides. *Spectrochim. Acta Part B At. Spectrosc.* **56**, 753–776 (2001).